Electrostatic Field-Based Multiscale Corner Detection: A Physics-Motivated Approach

Gamal Abdel-Hamid[1] and Yee-Hong Yang[2]

Computer Vision Laboratory, Department of Computational Science

University of Saskatchewan, Saskatoon, Saskatchewan, Canada S7N 0W0

Email Address for Y.H. Yang: yang@cs.usask.ca

Phone Number for Y.H. Yang: (306) 966-4891

Fax Number for Y.H. Yang: (306) 966-4884

December 14, 1994

Abstract

Corners represent special features of interest in images. They are very useful in many vision problems such as optical flow, structure from motion, and motion correspondence. A corner may be defined as the junction point between two or more straight line edges, or a point on the object's boundary curve having a curvature extremum. Our definition of a corner is a point having an electrostatic field extremum along an equipotential contour. Based on this definition, a novel approach for corner detection developed based on the electrostatic field theory *(EFT) is proposed. The approach, which is motivated by the simple observation that the electrostatic field is known to concentrate around pointed conductor edges, has the flavor of the multiscale-based approach of corner detection. In this paper, relevant background in EFT is reviewed. Corner detection using the proposed approach is then presented and demonstrated experimentally, the results of which are very encouraging and are used to demonstrate the potential and merits of the EFT-based approach.*

[1]Gamal Abdel-Hamid passed away on Dec. 4, 1994

[2]To whom correspondence should be addressed.

1 Introduction

Dominant points or corners represent special features of interest in images. They can abstract an object to a minimum number of points that best represent the shape of the object [4]. Therefore, they are of use in a wide range of vision problems including optical flow, structure from motion, motion correspondence, and polygonal approximation of objects among others. Many definitions of corners have been reported in the literature. Each definition of a corner yields a category of corner detectors. For example, in one definition, a corner is defined as the junction or intersection point of two or more straight line edges. The model-based optimal corner detector [20] and many other corner detectors have been developed based on this definition [8, 12, 13, 30]. Another more elaborate definition of a corner is a point along the object's boundary having a curvature extremum. The scale space approach of corner detection has been developed based on this definition [21].

In general, an ideal corner detector must possess the following characteristics:

1. The true corner points should be detected.

2. Corner points detected should be accurate in location.

3. The corner detector should be insensitive to noise.

4. False corner points must not be detected.

In this paper, a novel approach for corner detection based on the electrostatic field theory (EFT) is proposed [10, 14]. The new approach is motivated by the simple observation that surface charge density and the electrostatic field are known to concentrate on pointed ends of conductors [10]. This phenomenon has been exploited in many industrial applications requiring high electrostatic field. The lightning rod is also an application of this phenomenon. The idea is original and has not been reported in any published reports or papers [3]. Our investigation of the proposed corner detector shows clearly the potential and merits of the electrostatic field approach as compared with existing ones.

[3] An abridged version of this paper has been published in [1].

This paper is organized as follows. First, previous work done in corner detection is reviewed in Section 2. Relevant background on the Electrostatic Field Theory (EFT) is given in Section 3. The proposed EFT-based approach to corner detection is presented in Section 4. The experimental results on evaluating the proposed approach are presented in Section 5. In Section 6, conclusions and future work are discussed.

2 Previous Work

Although there are many proposed corner detectors, they can be classified into a small number of categories depending on the feature they utilize to detect corners. The first category uses the magnitude of the gradient of the gradient direction, at the point of interest as a measure of cornerness. This quantity attains a local maximum at a corner point [7, 8, 12, 13, 30]. This category of approaches has some disadvantages. First, the results are sensitive to noise. Secondly, a priori knowledge of the object size is required. Thirdly, even if the object or the feature size is supplied as an input parameter to the algorithm, the algorithm can not accommodate for objects having multiple-size features (for example, a door key, having a general shape as large feature and having teeth as fine feature). Lastly, this category of approaches is based on some edge model, which performs poorly at corners as reported by [11, 16].

The second category is based on the detection of half edges in an attempt to overcome the last problem mentioned above [16]. In this approach, a corner is defined more precisely as the intersection of two half edges. Eight half-edge detectors based on the first directional derivative of Gaussian are devised to detect half edges oriented at multiples of 45^0. The procedure works as follows. The eight half-edge detectors are applied to each pixel under study and the top two responses which exceed a preset threshold are taken. If the orientations of the two chosen half edges differ by a value other than 180^0, the pixel is declared as a candidate corner. Then, some criteria are applied to reduce the number of spurious corners. A major drawback of this category is that a sharp corner does not necessarily produce a high response. Also, this approach tends to favor corners of certain orientations and angles.

The third category uses a mathematical model-based approach and attempts to best fit the corner to the model [20]. The ratio of the signal-to-noise ratio (SNR) and the delocalization measure is used as a figure-of-merit to be maximized. The problem is then formulated as a maximization problem that is solved by means of the Euler-Lagrange equation, the solution of which is a template for matching with corner points. Eleven masks are devised to account for all corner configurations. Points giving a mask response beyond some thresholds are considered as candidate corners. Also some local criteria are used to eliminate false corner points. Although the approach seems rigorous, the performance of this corner detector is unsatisfactory especially when it is applied to real images [20].

The above three categories of approaches share some common problems. They can be described as low-level, mask-based, and single-scale corner detectors. The common problems associated with these categories are as follows. First, a priori knowledge of feature size is required. Second, no multiple scale capability is provided for objects having multiple size features. Third, they do not accommodate for round or curved corners.

The last category is trying to overcome problems associated with the aforementioned categories by introducing the notion of scale into corner detection. In this category, corners correspond to extrema of absolute curvature. Scale has been introduced gradually into corner detection schema. Sankar and Sharma [24] developed a parameter-free algorithm that utilizes multiple scale processing. In their schema, each boundary pixel is assigned a value of +1, -1, or 0 depending on its curvature if it is positive, negative, or zero, respectively. Then, iterative averaging of the assigned values at each pixel with its immediate neighbors is done and points with local maximum averaged values are marked as corners at the end of the iteration.

Teh and Chin [27] introduced a parameter-free algorithm that uses local curvature as in Rosenfeld-Johnson [22], Rosenfeld-Weazka [23], and Freeman-Davis [9], with the difference that the region of support for calculating the local curvature at each boundary pixel is adaptively determined based on the local properties of the pixel. Although the algorithm has shown to work well with objects having multiple-size features, the experimental results appear to be sensitive to quantization and boundary noise [21].

Asada and Brady [3] introduced the curvature primal sketch to represent changes in boundary curvature with scale. The primal sketch represents various symbolic descriptions of the object such as corners, knots, and ends at multiple scale. The sketch is constructed by convolving the curvature signal with Gaussian kernels of different scale σ. Corners are detected by tracking the locations of curvature discontinuities. A notion of best scale for a particular feature is defined, and, hence, boundary symbolic features are each detected at a different scale. The resulting representation is a multiple scale interpretation of the boundary; however, the detection of certain features is still based on the signal at a single scale.

A complete scale-based corner detector has been introduced by Rattarangsi and Chin [21] where the information of corners at different scales is integrated in a scale-space representation. The scale-space corner representation is generated by convolving the object's boundary functions $x(s)$ and $y(s)$ with a Gaussian filter of varying degrees of smoothing. Maxima of absolute curvature that persist under varying degrees of smoothing are declared as corner points. A rule-based tree-parsing algorithm is applied to the scale-space corner map to identify consistent maxima in this map. Experimentally, the performance of this approach was shown to compare favorably with other corner detectors, especially for objects possessing multiple scale features. One disadvantage of this approach is that several parameters have to be supplied to the algorithm, one of which is the largest degree of smoothing allowed (σ_{max}).

Our proposed approach for corner detection has the flavor of the scale-based approach [21]. The notion of scale, however, does not result from smoothing the object's boundary with Gaussian kernels of different σ, but rather, comes naturally as a result of solving the Poisson equation inside of the planar object. Our approach is developed based on the electrostatic field theory (EFT) and is motivated by the simple observation that the surface charge density and electrostatic field on conductors are known to be local maxima at points having curvature maxima, and minima at points having curvature minima [10] (see Figure 1, taken from [10]).

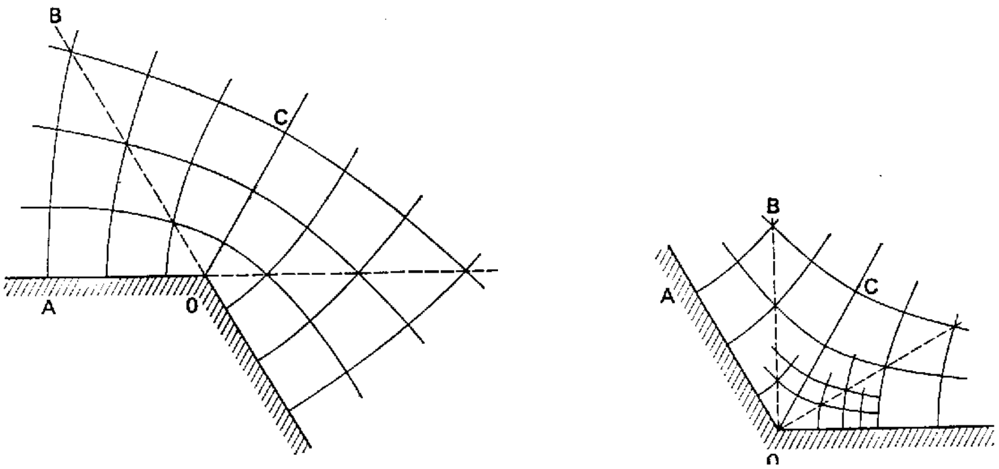

Figure 1: Equipotential and field lines near a corner : (a) Convex corner; (b) Concave corner. Note that equipotential line spacings are minimum(maximum) in case of convex(concave) corners along the corner bisector direction. This implies that the field is maximum(minimum) in case of convex (concave) corner along this direction (taken from [10]).

3 Background on Electrostatic Field Theory (EFT)

Relevant concepts in EFT are reviewed in this section. First, some basic concepts of the EFT are given. Then, the analytical equation that govern the electrostatic field near a corner is given. This is to present some intuition behind the idea of the approach.

3.1 Basic Concepts of the EFT

The following are some of the well-known properties governing the electrostatic potential and the electrostatic field:

1. The electrostatic potential, $v(x,y)$, at a point (x,y) in the 2-dimensional space R^2 is governed by the Poisson equation $\nabla^2 v = -\frac{\rho_{vf}}{\epsilon}$, where ∇^2 is the *Laplacian* operator given by $\frac{\partial^2}{\partial x^2} + \frac{\partial^2}{\partial y^2}$, ρ_{vf} is the free charge density at (x,y), and ϵ is the permittivity of the medium.

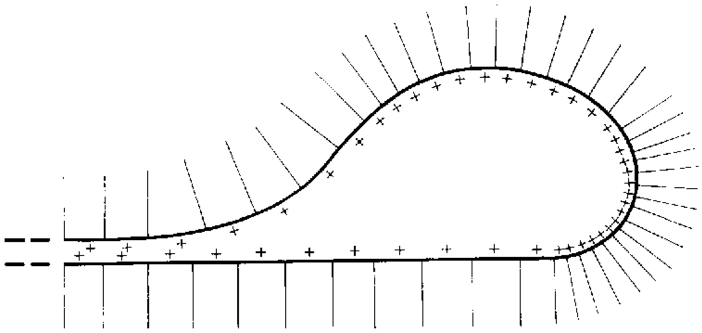

Figure 2: Charge and field distribution on the surface of a conductor. The field is highest at locations where the convex curvature is highest and the field is lowest at locations where the concave curvature is highest (taken from [10]).

2. The electrostatic field vector $\vec{E}(x, y)$ at (x, y) can be computed from the potential $v(x, y)$ using $\vec{E} = -\nabla v$. Two observations can be made. First, the field is in the direction of the steepest descent of the potential. Second, the field lines are perpendicular to the equipotential contours and are directed from the high to the low potential.

3. A pure conductor is an equipotential surface and the electrostatic field vector $\vec{E}$ is zero everywhere inside of the conductor. The electrostatic field on the conductor surface, however, may be nonzero and is given by$\vec{E_s} = \frac{\sigma_s}{\epsilon_0}\hat{n}$, where σ_s is the surface charge density, ϵ_0 is the permittivity, and $\hat{n}$ is an outward unit vector normal to the surface of the conductor.

4. The electrostatic field distribution on a conductor surface is related to the local curvature of the conductor surface and has been verified both theoretically [15] and experimentally [1], [10] (see Figure 2, taken from [10]). This means that the electrostatic field conveys the same information as the curvature of an object's boundary. The electrostatic field extrema along an equipotential contour correspond to curvature extrema or corners. This property is the main motivation behind the EFT-based approach.

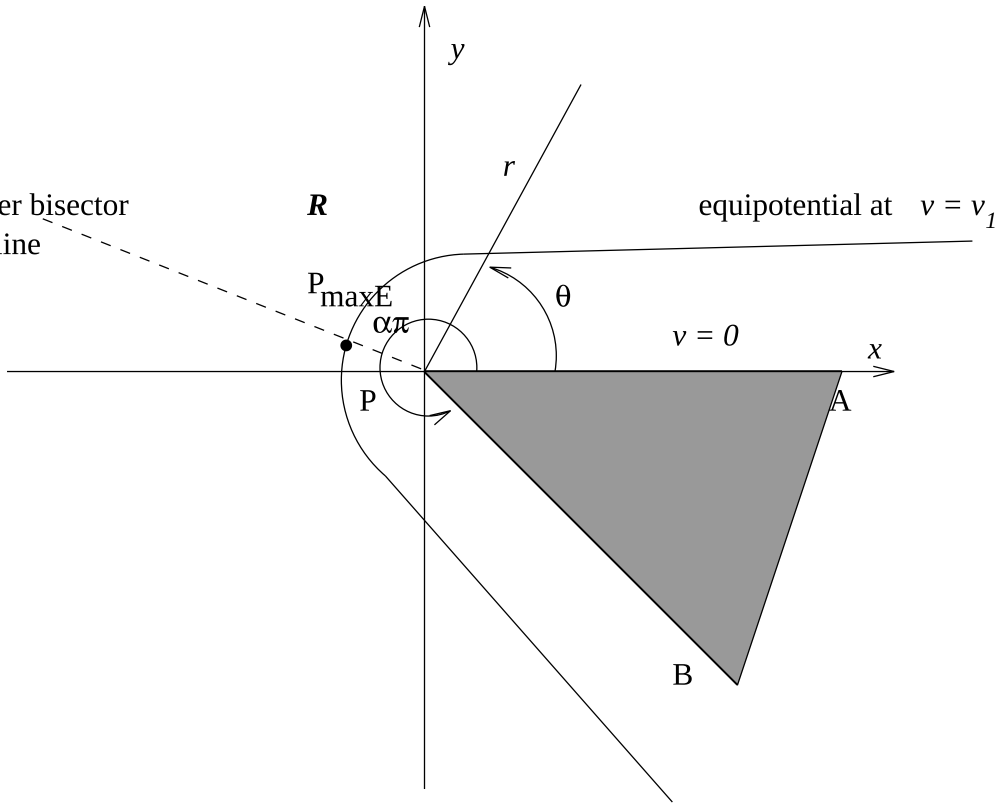

Figure 3: Geometry of an isolated planar knife-edge corner. PA and PB are the boundary lines kept at a potential 0. The external angle of the corner is $\alpha\pi$.

3.2 The Electrostatic Field Near a Corner

Figure 3 depicts an isolated planar knife-edge corner that is subtended by two straight lines PA and PB at angles 0 and $\alpha\pi$, respectively, where $1 < \alpha \leq 2$ (convex corners). The electrostatic potential in the region R, $0 \leq \theta \leq \alpha\pi$, is governed by the well-known Laplace equation. That is

$$\nabla^2 v = 0, \tag{1}$$

assuming a charge-free region R.

Solving the Laplace equation in the polar coordinate system (r, θ) under the boundary conditions: $v(\theta = 0) = v(\theta = \alpha\pi) = 0$, the potential function v can be expressed as [14]

$$v = \sum_{n=1}^{\infty} a_n r^{n/\alpha} sin(\frac{n\theta}{\alpha}). \tag{2}$$

Using the expressions :

$$\frac{\partial v}{\partial x} = \cos\theta \frac{\partial v}{\partial r} - \frac{\sin\theta}{r}\frac{\partial v}{\partial \theta}, \qquad \frac{\partial v}{\partial y} = \sin\theta \frac{\partial v}{\partial r} + \frac{\cos\theta}{r}\frac{\partial v}{\partial \theta}, \tag{3}$$

we find from Equation (2) that

$$\frac{\partial v}{\partial x} = \frac{-a_1}{r^\beta} \sin\beta\theta + O(r^{1-\beta}), \tag{4}$$

and

$$\frac{\partial v}{\partial y} = \frac{a_1}{r^\beta} \cos\beta\theta + O(r^{1-\beta}), \tag{5}$$

where $\beta = 1 - \frac{1}{\alpha}$. Consequently, if $\alpha > 1$, both $\frac{\partial v}{\partial x}$ and $\frac{\partial v}{\partial y}$ tend to infinity as $r \to 0$. That is to say, there is a boundary singularity of the field at $P(r = 0)$. In corners having smoother curvature, the field is no longer infinite but is still much higher than anywhere else on the conductor surface.

Considering only the first terms in equations (4) and (5) for simplicity (i.e. the dominant mode), the magnitude of the electrostatic field can be expressed as

$$|\vec{E}| = |-\nabla v| = \frac{a_1}{r^\beta}. \tag{6}$$

Consider a contour of constant potential (equipotential) $v_1 > 0$ as shown in Figure 3. For such an equipotential

$$v_1 = a_1 r^{1/\alpha} \sin(\frac{\theta}{\alpha}), \tag{7}$$

which yields r in this equipotential as

$$r = \frac{v_1^\alpha}{a_1^\alpha \sin^\alpha(\frac{\theta}{\alpha})}. \tag{8}$$

Manipulating for $|\vec{E}|$ on the equipotential at $v = v_1$ gives

$$|\vec{E}| = \frac{a_1^\alpha \sin^{\alpha-1}(\frac{\theta}{\alpha})}{v_1^{\alpha-1}}. \tag{9}$$

The direction of the field vector, θ_E, is given by

$$\tan(\theta_E) = \frac{E_y}{E_x} = \frac{-\frac{\partial v}{\partial y}}{-\frac{\partial v}{\partial x}} = -\cot(\beta\theta) \tag{10}$$

or

$$\theta_E = \beta\theta - \frac{\pi}{2}. \tag{11}$$

For given v_1 and α, the electric field along the equipotential line attains a maximum at the point P_{maxE} in the direction $\theta = \frac{\alpha\pi}{2}$, which is the direction of the angle bisector as shown in Figure 3. Thus, the maxima of field along an equipotential contour can be used as indicators for corners. The direction of the field vector at P_{maxE} is also along the bisector line as can be easily seen when substituting $\theta = \frac{\alpha\pi}{2}$ in Equation (11) above. This means that the maximum field is pointing towards the corner. This is for convex corners.

For concave corners ($0 < \alpha < 1$), similar argument is still valid, but with field minima instead of maxima. Equation (9) can still be used, with $0 < \alpha < 1$. The direction of field minimum also coincides with the corner bisector.

This property of the equipotential contour or line is very important and suggests that corners of an object can be detected using the EFT at a distance away from the corner position. Also, corners of noisy objects can be robustly detected since along an equipotential at a distance from the object's boundary the field variation is less severe than that at the object's boundary.

4 The EFT-Based Corner Detector

This section discusses how the ideas given in Section 3 are implemented to form our EFT-based corner detector. Figure 4 depicts the steps that compose the proposed corner detector.

Given the input binary image of a planar object, the first step computes the potential distribution inside of the object. Starting from the potential distribution of the object, the second step builds a scale-space corner tree of the object using the potential as the scale. In the third step, the task is to trace the corners detected at a given scale (i.e. equipotential) down to the leaves of the scale-space corner tree. This step gives the initial corners locations, that is, corners along the lowest potential equipotential in the scale-space corner tree. Using the initial corners, the fourth step locates corners along the object's boundary by shooting at the boundary from the initial corners' positions in the field direction. The following subsections give the details of the above steps.

4.1 The Potential Distribution Inside the Object

Abdel-Hamid and Yang [1] introduced the EFT-based approach to detect corners in the following way. The planar object is modeled as an equipotential of a potential v_{object} and the image rectangular border as another equipotential of a potential $v_{border} \neq v_{object}$ and the Laplace equation is then solved in the region between the two equipotentials to give the potential distribution outside of the object. This problem is the *Exterior Dirichlet Boundary Problem* [26]. Although that model is good enough to demonstrate the idea of using the EFT to detect corners, thorough investigation of the model showed that it exhibited a number of problems. First, the interaction between the border of the image and the object is ignored. Hence, the applicability of the model is limited to objects which are small in comparison with the image size. Second, rotation, displacement, and/or scaling of the object would definitely have an effect on the resulting potential distribution. These problems can be addressed, however, if the potential distribution is computed inside of the object instead of outside of it. This problem then becomes the *Interior Dirichlet Boundary Problem*, which is the approach to be discussed in this paper. The Interior Dirichlet Boundary Problem has a unique solution for given boundary conditions and charge distribution [26]. If the Laplace equation is solved inside of the object (i.e. charge-free interior region), the potential distribution will be uniform. In our proposed approach, however, the interior region of the object is charged with a positive uniform charge density ρ_f so that the potential

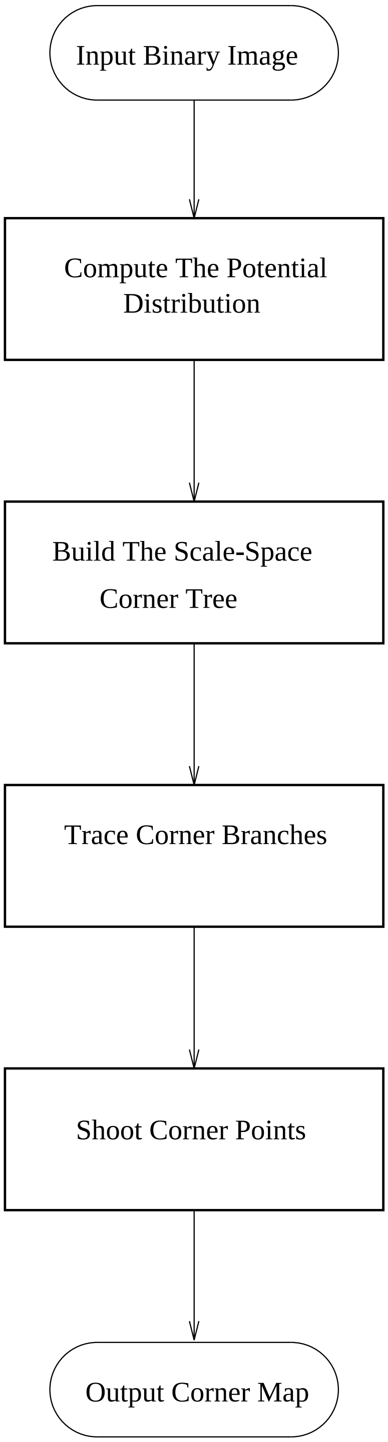

Figure 4: The steps of the EFT-based corner detection approach.

variation induced by the charge distribution will be solely due to the object's shape. The object's boundary is kept at a potential of zero and the Poisson equation is solved inside of the object. Many numerical methods can be used to solve the Poisson equation [5]. In our approach, the finite difference method with Richardson's relaxation [5] is used for its simplicity. The potential at pixel (i, j) inside of the object is computed iteratively using the following expression:

$$v_{i,j}^k = \frac{1}{4}(v_{i+1,j}^{k-1} + v_{i-1,j}^{k-1} + v_{i,j+1}^{k-1} + v_{i,j-1}^{k-1} + \frac{\rho_f}{\epsilon}),$$

where $v_{i,j}^k$ represents the potential at pixel (i, j) at the kth iteration. The process converges to a final solution when an error measure is less than a pre-defined threshold, ϵ, after a number of iterations m as follows:

$$\sum_{i,j} |v_{i,j}^m - v_{i,j}^{m-1}| < \epsilon.$$

The values of $v_{i,j}$ are expressed as floating point numbers. In the implementation, ϵ is set equal to 10^{-6} and for this value of ϵ, a typical value of m is in the order of $10,000$ iterations. In our implementation and the images used, this number of iterations takes about 20 minutes on a Sun SPARCstation 10. Figure 5(a) depicts the potential distribution or surface generated for a Maple leaf. It can be clearly seen that the potential is monotonically increasing as one goes deeper into the object in the direction of the potential gradient. Also, the potential gradient is steepest near concave corners and lowest near convex corners. The potential distribution attains its peak at the center of the object. It is important to note that the value of the charge density ρ_f does not affect the potential distribution except for a linear scale value. This is due to the linearity of the Poisson equation. Hence, the potential distribution is a characteristic of the object and any value of ρ_f can be used to find the distribution $v_{i,j}$ and then a simple linear transformation is done to normalize the potential distribution so that the peak of the distribution has a fixed value. In this paper, a value of 255 is chosen as the peak potential and the other potential values $v_{i,j}$ are normalized accordingly.

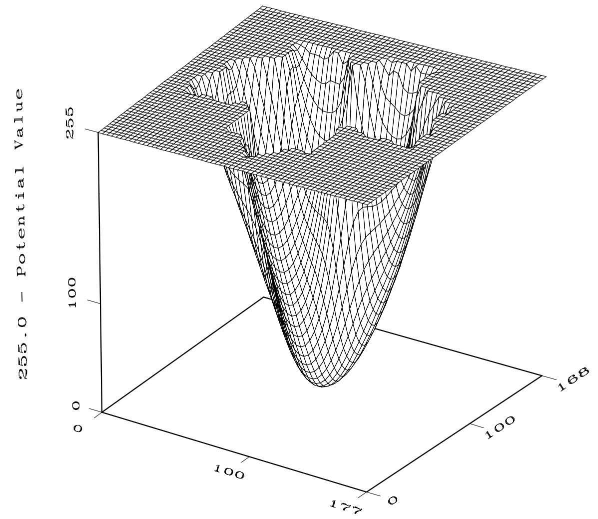

Figure 5: The potential distribution or surface generated for the image of a Maple leaf. The surface is inverted to show better.

4.2 Construction of the Scale-Space Corner Tree

Given the potential distribution or surface of the object produced in the previous step, the task of this step is to build the scale-space corner tree of the object. In this paper, the notion of scale corresponds to the potential value of an equipotential contour. This means that the constant scale curve is the equipotential contour. Recall from Section 3 that corners in the proposed EFT-based corner detection approach correspond to points having field extrema along equipotential contours. Hence, this step of the algorithm can be decomposed into two substeps; first, build the equipotential contours for the object; second, detect points of field extrema along the equipotential contours.

4.2.1 Construction of the Equipotential Contours

The equipotential contours are constructed for a potential range from v_{low} to v_{high} at a uniform step of v_{step}, where $0 < v_{low} < v_{high} < 255$. Each of the equipotential contours represents the object at a different level of detail. As the potential value of the contour increases, some of the object's details disappear.

This substep can be visualized as a potential surface, $S = v(x, y)$, being cut by constant potential planes (parallel to the x-y plane). The curve that results from the intersection of the potential surface and a cutting plane is a closed contour. In the implementation, the contour is expressed as a Freeman chain code. Since the spatial domain is a digital grid and the potential distribution takes on floating point values, the construction of a connected equipotential contour at a given potential, v_{con}, $v_{low} \leq v_{con} \leq v_{high}$, can be computed as follows.

First, all pixels having a potential greater than or equal to v_{con} are marked. The marked region is guaranteed to be a single connected region. Second, the boundary of the marked region is traced in the clockwise direction and these boundary pixels are labeled in Freeman chain code. As the boundary is traversed, the location, at subpixel resolution, of the point at which the potential is exactly equal to v_{con} is found by using bilinear interpolation (see [6] for details). By connecting the locations (at subpixel resolution) having a potential exactly equal to v_{con}, the required equipotential contour is constructed. The corresponding field values at each of this chain of points are also computed simultaneously for the next substep. In this way, the one-dimensional relation between the field, $E_{v_{con}}$, along each contour and the corresponding arc length, $s_{v_{con}}$, measured with reference to an arbitrarily chosen point on the contour, is found. The total length of the contour is normalized to 1. Thus, the result of this step is a set of one-dimensional curves $\{E_{v_{con}}(s) : v_{con} \in [v_{low}, v_{low} + v_{step}, \cdots, v_{high}]\}$. Since the field extrema along the equipotential contours are to be matched in the subsequent steps of the EFT-based corner detector, a reference line at which $s = 0$ must be found. Such a reference line should be crossing the equipotential contours at right angles, and hence, is a field line. This field line can be found by the following procedure. A pixel is selected arbitrarily on the object's boundary. A negative point charge is put on the pixel location and the field line is traced by the path of motion of the negative charge. The charge moves in the direction of the potential gradient, i.e. the direction of steepest ascent, until it hits the top or the peak of the potential surface. The intersections of this field line with the equipotential contours represent the $s = 0$ points for all the equipotential contours. The equipotential contours for the image of the Maple leaf are illustrated in Figure 6 along with

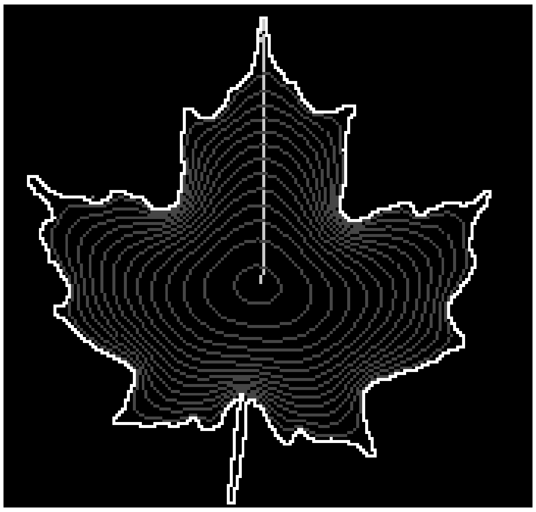

Figure 6: Construction of the equipotential contours in the EFT-based approach. Equipotential contours are constructed for the Maple leaf in Figure 2. The bright contour is the square's boundary. The gray contours are the equipotential contours. The reference field line ($s = 0$ line) is also shown cutting the contours. The equipotential contours shown are constructed in the potential range 10-250 in steps of 20. When the contour is closer to the center of the object, the contour gets smoother and details tend to disappear.

the reference field line.

It is noteworthy that the lower is the value of contour potential, v_{con}, the smoother the contour, the smoother the curve $E(s)$, the less the number of field extrema, and the less the number of corners as expected due to the smoothing effect of the solution of the potential distribution inside of the object. Figure 7 illustrates this effect by depicting the field distribution along different equipotential contours for the image of a Maple leaf with the boundary corrupted with Gaussian noise of $\sigma = 1.0$.

Another finding regarding the equipotential contours is the relationship between the field and the curvature which confirms Concept 4 as discussed in Section 3. The curvature distribution along some equipotential contours of the noise-corrupted Maple leaf corresponding to the field distributions along the same equipotentials shown in Figure 7 is illustrated in Figure 8.

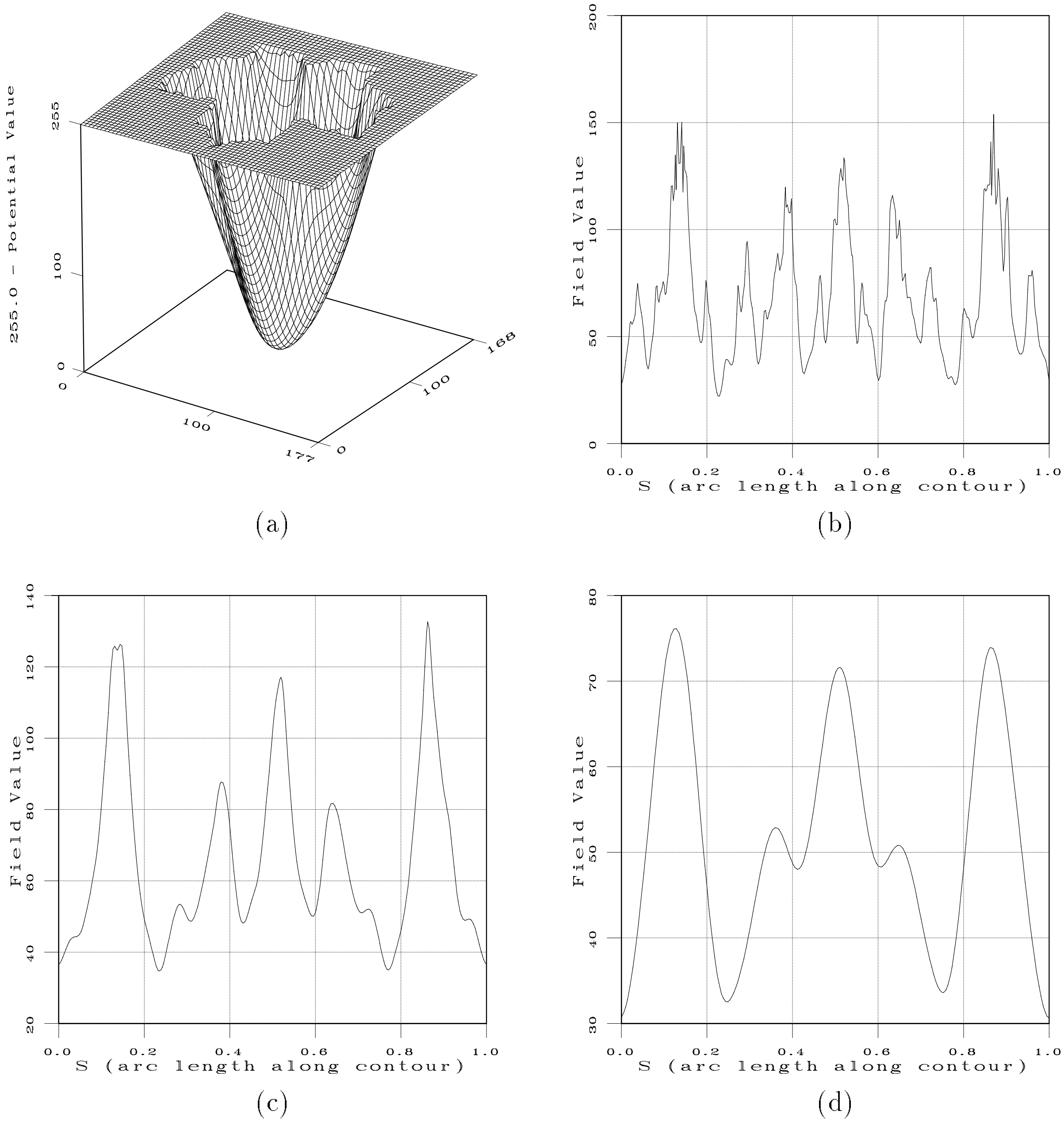

Figure 7: The smoothing effect on field magnitude at equipotential contours. (a) The potential surface generated for a Maple leaf with boundary corrupted by Gaussian noise of $\sigma = 1$; (b)-(d) Field distribution along equipotential contours of potentials = 20, 75, and 150, respectively. Notice that, the lower the potential, the less the number of field extrema (corresponding to significant convexities and concavities). This illustrates the multiple scale capability of the proposed approach.

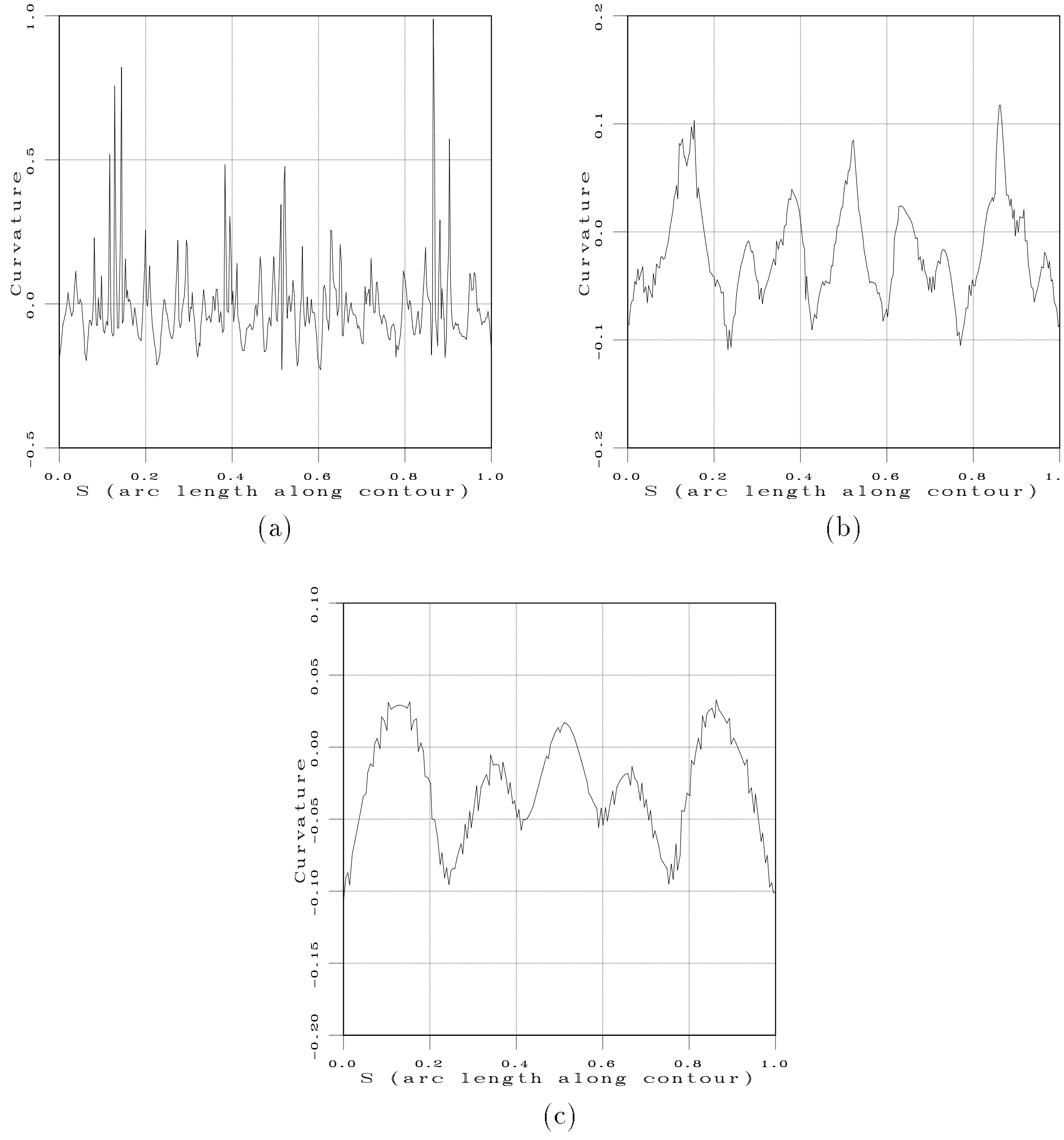

Figure 8: The curvature signal along equipotential contours. The figures correspond to the variation of curvature along the equipotential contours shown in Figure 7. The field and curvature signals correlate very clearly.

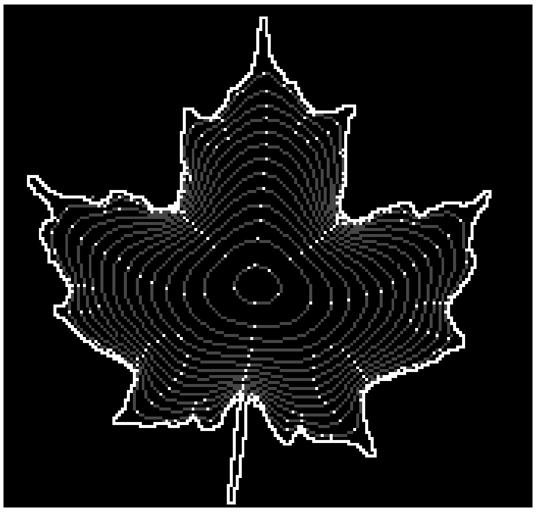

Figure 9: Detection of field extrema along equipotential contours. Notice that not all detected field extrema correspond to true corners.

4.2.2 Detecting Corners along the Equipotential Contours

The field distribution along each of the equipotential contours constructed in the last substep contains information relevant to corner detection. Recall that our definition of a corner is a point having a local field extremum along some equipotential contour. Field minima correspond to convex corners and field maxima correspond to concave corners. Field local extrema are detected by a simple search method. Field extrema detected for the image of the Maple leaf are shown in Figure 9. Not all field extrema correspond to true corners. Any pair of adjacent minima corresponding to a pair of convex corners encompasses one field minimum and vice versa. This field minimum can be just a transition between two maxima and does not necessarily correspond to a corner. Field extrema that do not correspond to true corners have to be eliminated. This problem is similar to taking *curvature extrema* rather than *absolute curvature extrema* as corners in the curvature-based corner detectors [21]. Since the field magnitude along an equipotential contour does not have a polarity or a sign, another way of eliminating these false corners is needed. The *true convexity-concavity* test is a test done for every field maximum and minimum to filter out the false corners as follows. First, for each field extremum, a region of support is defined and found as in [21]. Let the left and right ends of the region of support be denoted p_l and p_r, respectively. Let

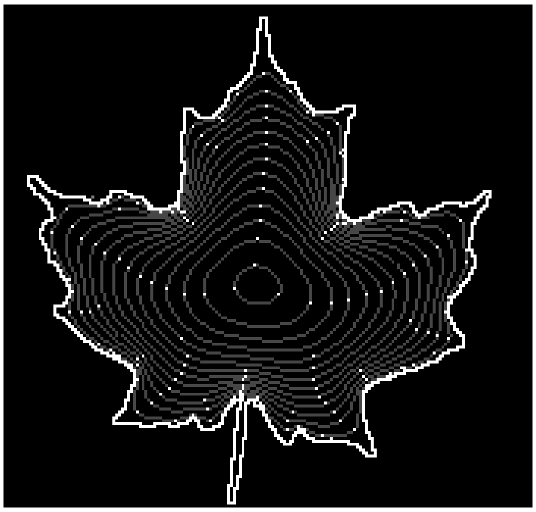

Figure 10: The output of the second step of the EFT-based corner detector. Figure shows corners detected after passing the convexity-concavity test. False corners are all removed by the test. The equipotential contours are the same as those depicted in Figure 6.

the point corresponding to the field extremum be p_i. Assume that the contour is traversed in the clockwise direction. For a field minimum to be a convex corner, the cross product of the two vectors $\vec{p_i} - \vec{p_l}$ and $\vec{p_r} - \vec{p_i}$ must give rise to a rotation in the clockwise direction or a positive cross product as follows:

$$(\vec{p_i} - \vec{p_l}) \times (\vec{p_r} - \vec{p_i}) > 0.$$

Similarly, for a field maximum to be a concave corner, the cross product of the two vectors $\vec{p_i} - \vec{p_l}$ and $\vec{p_r} - \vec{p_i}$ must give rise to a rotation in the counterclockwise direction or a negative cross product as follows:

$$(\vec{p_i} - \vec{p_l}) \times (\vec{p_r} - \vec{p_i}) < 0.$$

Field extrema violating these conditions are excluded. Note that the convexity-concavity test does not involve any thresholding parameter and involves just a sign test which is not sensitive to noise. Figure 10 illustrates the corners detected in Figure 9 after passing the convexity-concavity test. All false corners are removed by the test.

The output of this step of the algorithm is a scale-space representation of corners de-

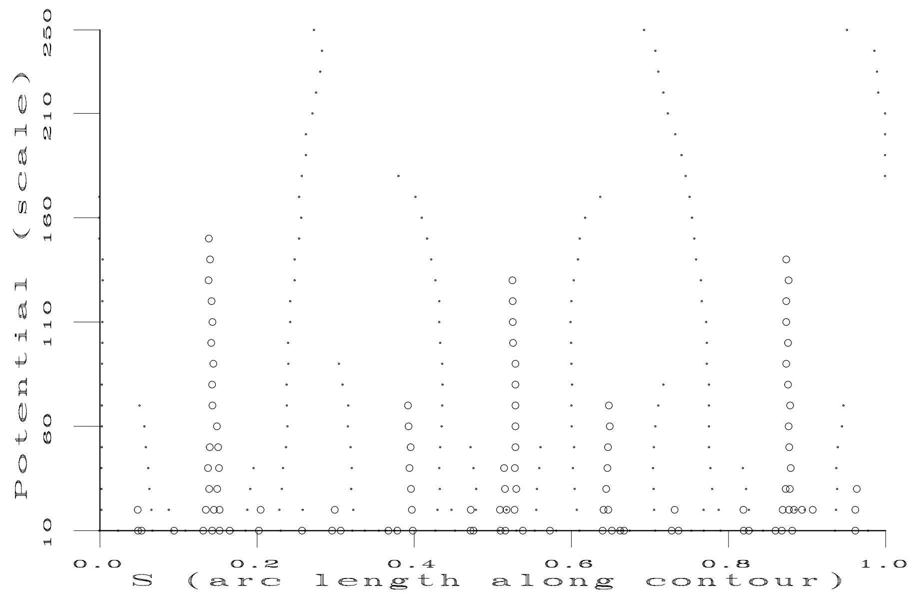

Figure 11: The output of the second step of the EFT-based corner detector. The scale-space corner representation of the Maple leaf. In the figure, $v_{low} = 10, v_{high} = 250$, and $v_{step} = 10$. The locations of convex corners are shown as dots and the locations of concave corners are shown as circles.

tected along the equipotential contours. The potential value of the equipotential contour represents the scale and the space parameter s denotes the normalized arc length along the equipotential contour. The scale-space corner tree of the Maple leaf is depicted in Figure 11. The representation is similar to that generated by the approach in [21].

4.3 Traversing the Scale-Space Corner Tree

Given the complete scale-space representation of corners, it is usually desired to detect corners of the object as viewed at a certain level of detail or scale. Therefore, this step of the algorithm starts at a potential v_{start} at which corners are detected. v_{start} is a user-supplied parameter to the algorithm that determines the level of detail desired for the corner representation of the object. Selecting a high value of v_{start} a coarse corner representation is produced and vice versa. Our approach for tracing corners along the tree branches can be considered as a top-down approach. Initially, corners are detected at a rather coarse scale, v_{start}, final corners are located at the finest possible scale. This is achieved by the following procedure. Corners detected at the starting potential, v_{start}, are matched with their corresponding corners at an adjacent potential, $v_{start} - v_{step}$. Every corner at v_{start} is matched with the closest corner in s of the same type (convex or concave) at $v_{start} - v_{step}$. This yields new corners at a lower scale and closer spatial location to the object's boundary. The new set of corners are matched with corners at the lower scale of a potential of $v_{start} - 2 * v_{step}$. This process is repeated until corners are located at the lowest scale in the scale-space representation at a potential of v_{low}. The procedure is depicted in Figure 12 for part of the scale-space representation of the Maple leaf.

In case of a branching corner (i.e. two convex or two concave corners merged at a higher scale), the new corner location is taken as the middle point (in s) between the two corners. This is reasonable because neither of the two corners is more preferable than the other. The end product of this step is the location of corners traced down to the lowest scale at the potential, v_{low}. The corner locations are referred to as the *initial* corner locations. This is illustrated in Figure 13 for the image of the Maple leaf.

It is important to note that in edge and corner detection, there is a well-known tradeoff between noise immunity and location accuracy of the detected features. Our approach, however, does not suffer from this problem since corners are detected at a coarse scale but located at a fine scale.

4.4 Shooting Corner Points

It was found through experiments that tracing the corners down the scale-space representation up to the object's boundary (i.e. having $v_{low} = 0$) would locate corners inaccurately. Therefore, the tracing step (see last subsection) ends at a potential $v_{low} > 0$, and corners are located afterwards on the object's boundary using another method that yields more accurate results. The method works as follows. For every initial corner location found from the last step, the object's boundary is shot at from the initial corner location in the direction of the field, i.e. the direction of steepest descent. The pixel on the object's boundary first hit by this straight line shot is marked as the final corner position. Figure 14 depicts the shooting

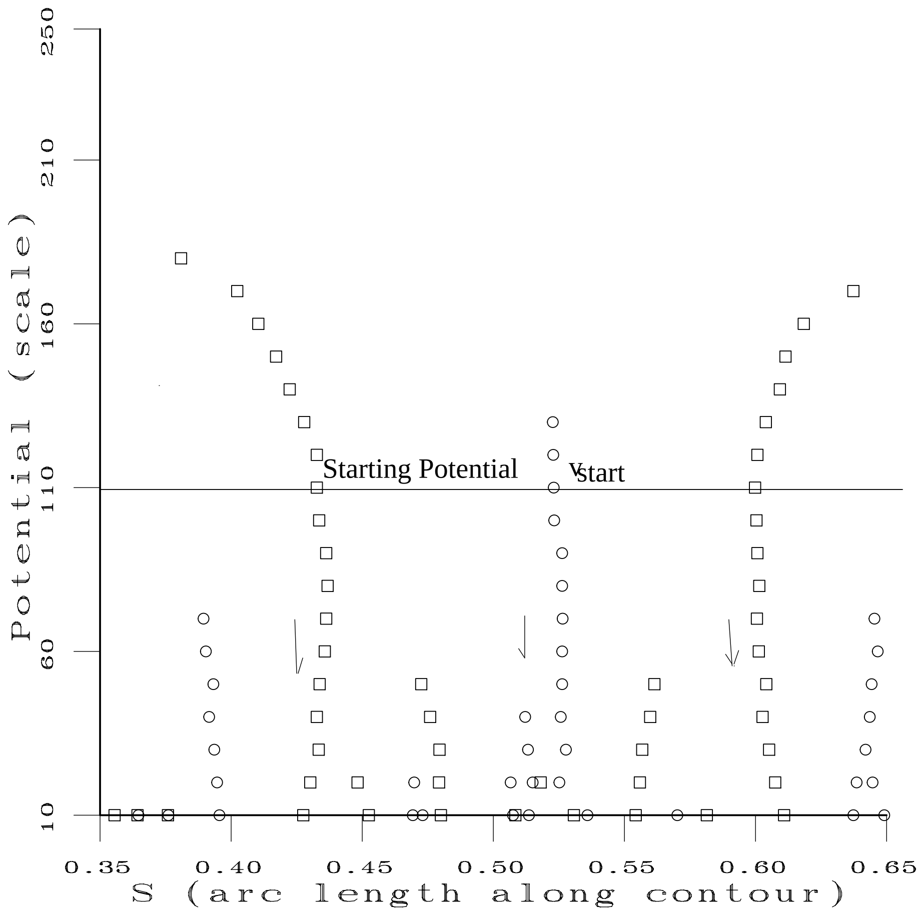

Figure 12: The third step of the EFT-based approach. Tracing corners down the scale-space map up to the leaves. Figure shows part of the scale-space corner map illustrated in Figure 11. $v_{start} = 110$ and $v_{low} = 10$

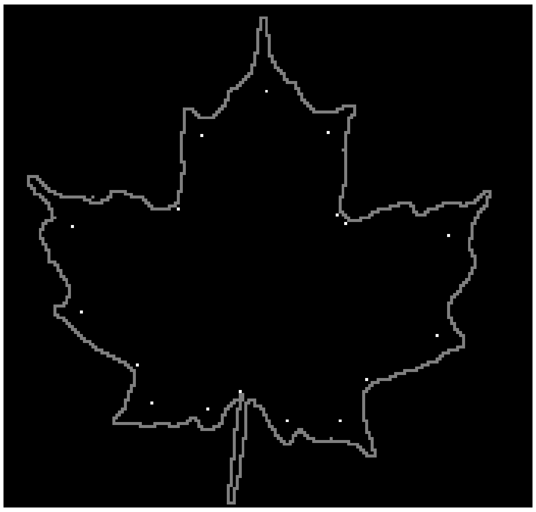

Figure 13: The output of the third step of EFT-based approach. The initial corners are shown as bright dots. The corners are detected at $v_{start} = 50$ and traced up to $v_{low} = 30$.

step of the algorithm for the image of the Maple leaf. In this figure, starting corners are detected at a starting potential of $v_{start} = 105$ and the boundary is shot at from a potential of $v_{low} = 5$.

5 Experimental Results

The proposed EFT-based corner detection schema has been tested with a large number of synthetic and real images to investigate the different aspects of the corner detection process. In this section, the results of some of the experiments are presented.

5.1 Simple Geometric Shapes

The first set of images consists of simple synthetic geometric shapes having well-defined corners. The purpose of this experiment is to study the performance of the proposed corner detector with respect to its sensitivity to the angle and orientation of the corner and quantization noise. Figure 15 depicts the results of an experiment on a 128×128 image of a 105×64 rectangle. The scale-space corner map of the rectangle is illustrated in Figure 15(a). Notice that pairs of corners are merged at 200. Corners are detected accurately and

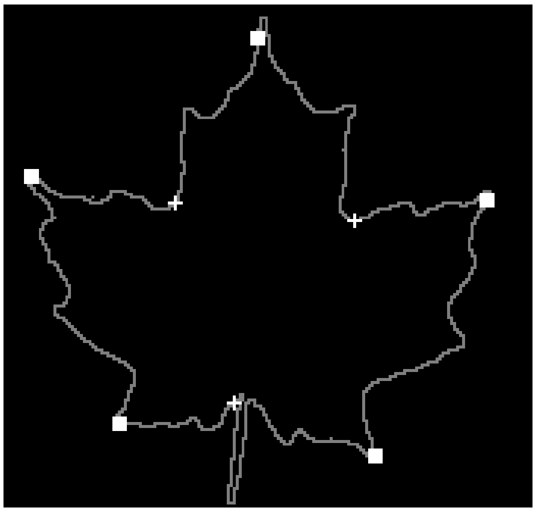

Figure 14: The final step of the EFT-based corner detection approach. Boundary is shot at from a potential of 5 (v_{low}). Starting corners are detected at a potential of 105 (v_{start}). The interpotential step of the scale-space representation (v_{step}) is 10. A convex corner is marked by a square and a concave corner is marked by a cross.

the result is shown in Figure 15(b) and (c). Another experiment was conducted on an image of a polygon with corners of different angles and orientations to test the impact of quantization noise on the performance of the proposed corner detector. The results are depicted in Figure 16. The scale-space corner map is shown in Figure 16(a). It can be seen that a large number of corners which exist in the scale-space map at a low potential, cease to exist at a higher potential. The corners detected are shown in Figure 16(b). It can be seen that when the corners are not very acutely convex, the corners are accurately located. When the corners are acutely convex as in the case of the bottom two corners shown in Figure 16(b), there is an error in the location. The reason is mainly due to the quantization of the digital grid and the accuracy in computing the field direction when the initial corner is near the boundary.

5.2 Accuracy and Noise Sensitivity

The purpose of this experiment is to investigate the performance of the proposed corner detector under the impact of boundary noise. The boundary of a 64×64 pixels square in

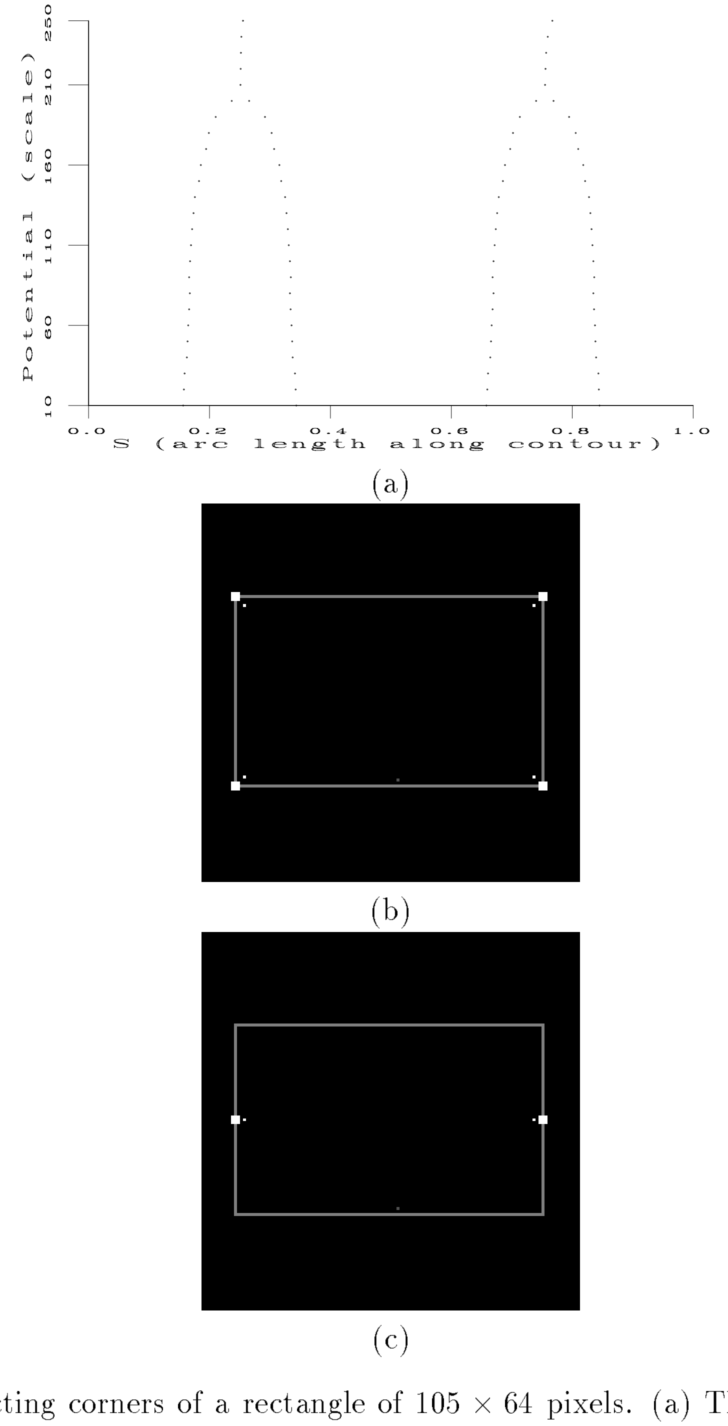

Figure 15: Detecting corners of a rectangle of 105 $\times$ 64 pixels. (a) The scale-space corner map for the rectangle. Notice that two pairs of corners merge at a potential of 200. (b) Corners detected with $v_{start} = 20$. (c) Corners detected with $v_{start} = 220$.

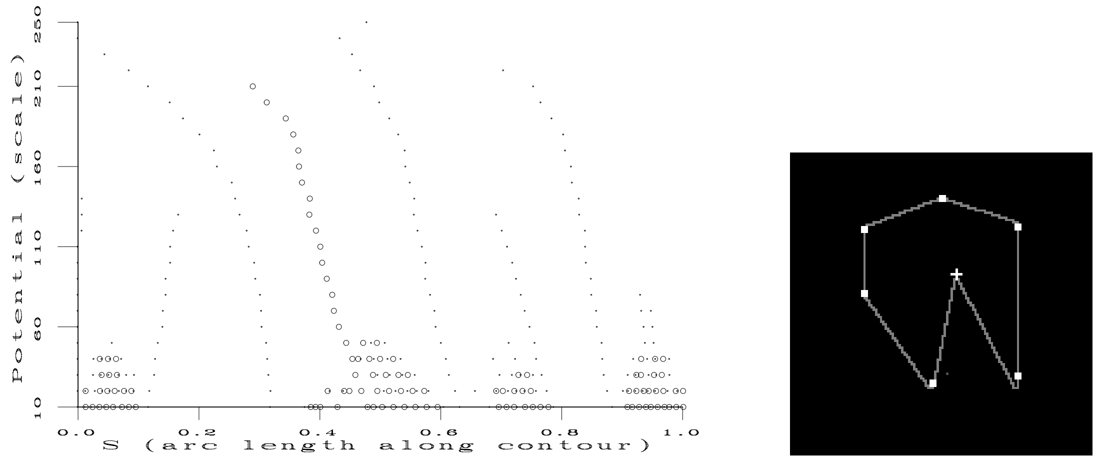

(a) (b)

Figure 16: An experiment on a polygon containing 6 convex corners and 1 concave corner. (a) The scale-space corner map for the polygon. (b) Corners detected are shown marked and superimposed with the boundary of the object. For this figure, $v_{start} = 100$ and $v_{low} = 20$.

a 128×128 image has been corrupted systematically by a zero-mean white Gaussian noise of varying σ_N. The noise is rounded off to the nearest integer and added to the boundary. Figure 17 shows the results of the square corrupted with a Gaussian noise of $\sigma_N = 0, 2.0$, and 4.0. Corners are detected at a potential of 220 and the boundary is shot at from a potential of 10. The experiment is conducted systematically for a set of Gaussian corrupted boundaries with σ_N in the range of 0 to 4.0 in steps of 0.2. The corners are detected at a potential (v_{start}) of 220 and the boundary is shot at different values of v_{low}. v_{low} is varied in the range of 5 to 100 in steps of 5. The corners are located and the average distance measured between the location of the detected corners and the ideal corners' locations (the locations of corners in the noise-free square) is computed. The results are plotted in a 3-D surface shown in Figure 18. From the figure, one can observe that the inaccuracy in the location of the corner is proportional to the noise level. Also, for large noise levels, choosing a high value of v_{low} results in a better accuracy of the corner location. This can be explained as follows. The noise smoothing effect increases with the potential, v_{low}, and, hence, the tracing of corners along the scale-space corner map should stop at a higher value of v_{low}.

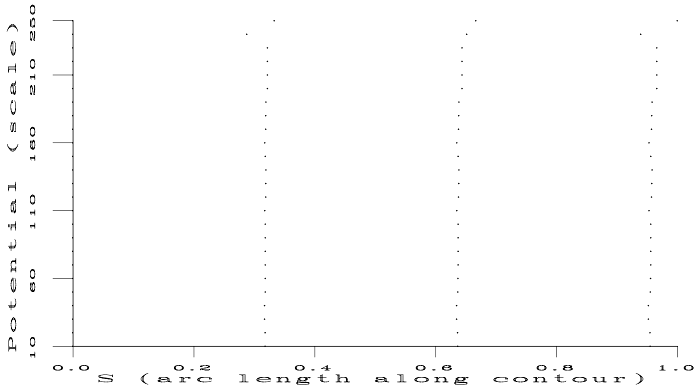

(a)

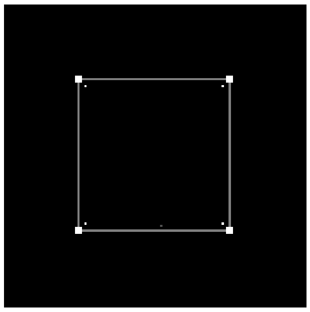

(b)

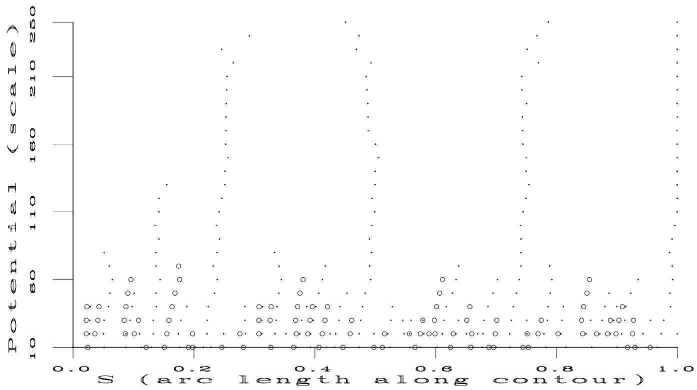

(c)

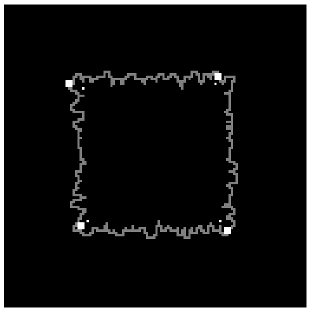

(d)

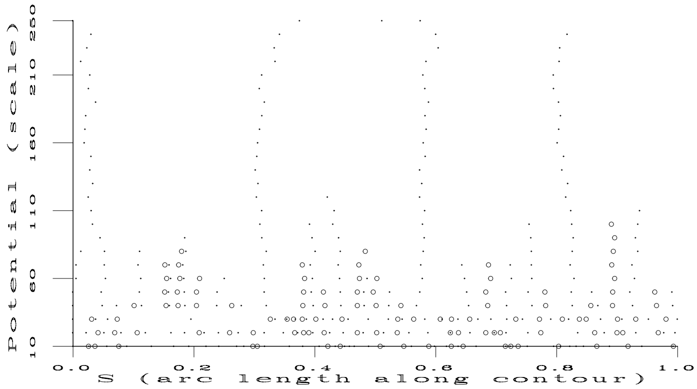

(e)

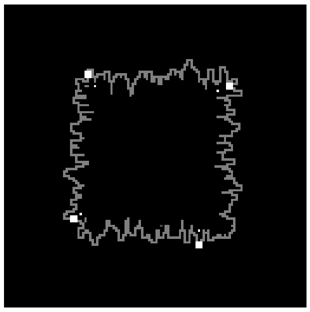

(f)

Figure 17: The impact of boundary noise on the performance of the EFT-based approach. (a) The scale-space corner map for a noise-free square (b). (c) The scale-space corner map for a square corrupted with Gaussian noise of $\sigma_N = 2.0$ (d). (e) The scale-space corner map for a square corrupted with Gaussian noise of $\sigma_N = 4.0$ (f). The corners are detected at a potential of 220 and the boundary is shot at from a potential of 10.

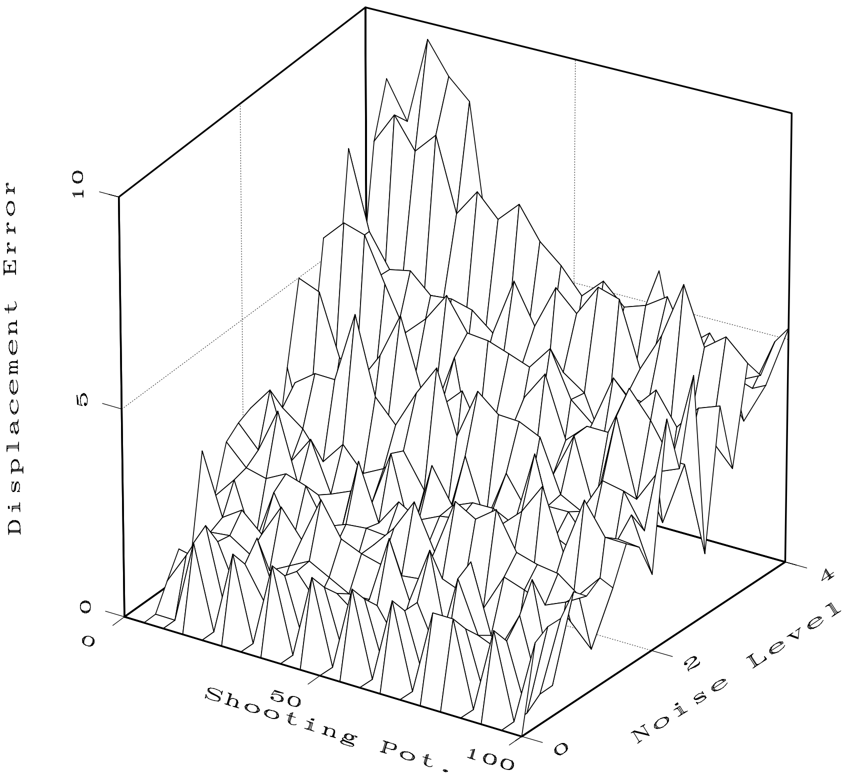

Figure 18: The accuracy of corner location for the EFT-based corner detector. The average displacement of corners plotted against the shooting potential and the noise level. The inaccuracy increases with the noise level. Choosing a higher shooting potential for very noisy images results in better location of corners.

5.3 The Multiscale Capability

It is believed that the best scale of an object cannot be determined automatically. In fact, every object can be viewed differently at different levels of details. Details may be overlooked at some scale depending on the interpretation required. The purpose of this experiment is to illustrate that the EFT-based corner detector is able to detect corners of objects at different levels of detail. Figure 19 depicts the results of applying the EFT-based approach to an image of a Maple leaf where corners are detected at different potentials v_{start}. Figure 19(a), (b), and (c) show the scale-space corner map, corners detected at $v_{start} = 100$ and 30, respectively. A coarse scale description of corners is obtained at $v_{start} = 100$ and a finer scale description of corners is obtained at $v_{start} = 30$.

5.4 Comparison with Related work

The purpose of this experiment is to compare our results with some of the related work in corner detection. The first experiment is an image of a digital ellipse with the major and minor axes of 70 and 35, respectively, and the results are shown in Figure 20. The results can be compared to the results given in [21](Figure 20 in [21]). The results illustrate the robustness of the EFT-based approach and its insensitivity to quantization noise. Another experiment is done on an object digitized from [21]. The results of applying the EFT-based approach are shown in Figure 21. It can be seen that the results using our proposed approach compare favorably with those shown in Figure 22 in [21].

6 Conclusions and Future Work

In this paper, a novel corner detection approach developed based on the Electrostatic Field Theory (EFT) is proposed. Related work in corner detection has been reviewed. Relevant background on the EFT has been given and a new definition of a corner has been proposed. In the EFT-based approach, a corner is defined as a point along an equipotential contour having a field extremum. Based on this definition, the object's boundary is modeled as an equipotential of zero potential and the object interior is charged with uniform charge

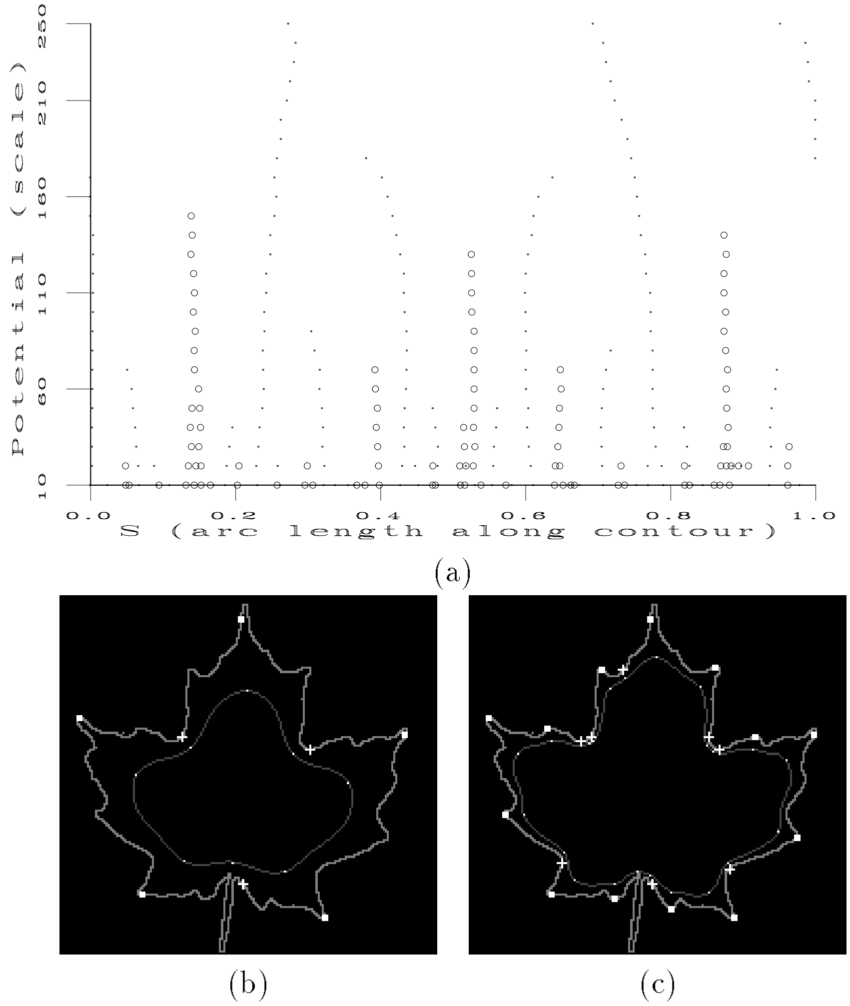

Figure 19: The multiscale property of the EFT-based approach. (a) The scale-space corner map of the Maple leaf. (b) and (c) Corners detected at $v_{start} = 100$ and 30, respectively. (c) reflects the Maple leaf at a coarse scale and (c) reflects the Maple leaf at a fine scale. In (b) 5 convex corners and 3 concave corners are detected whereas in (c) 13 convex corners and 6 concave corners are detected. The equipotential contours at v_{start} are also shown.

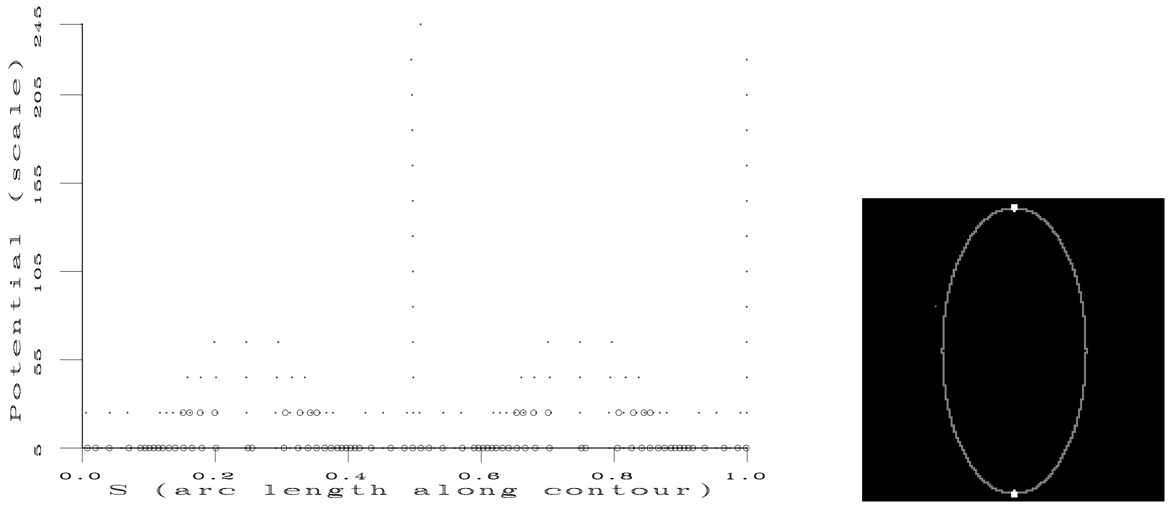

(a) (b)

Figure 20: Comparison with related work. A digital ellipse of 70 and 35 pixels major and minor axes, respectively. (a) the scale-space corner map of the digital ellipse. (b) Corners detected. Only two convex corners are detected. Results compare favorable with results given in [21](Figure 20 in [21]).

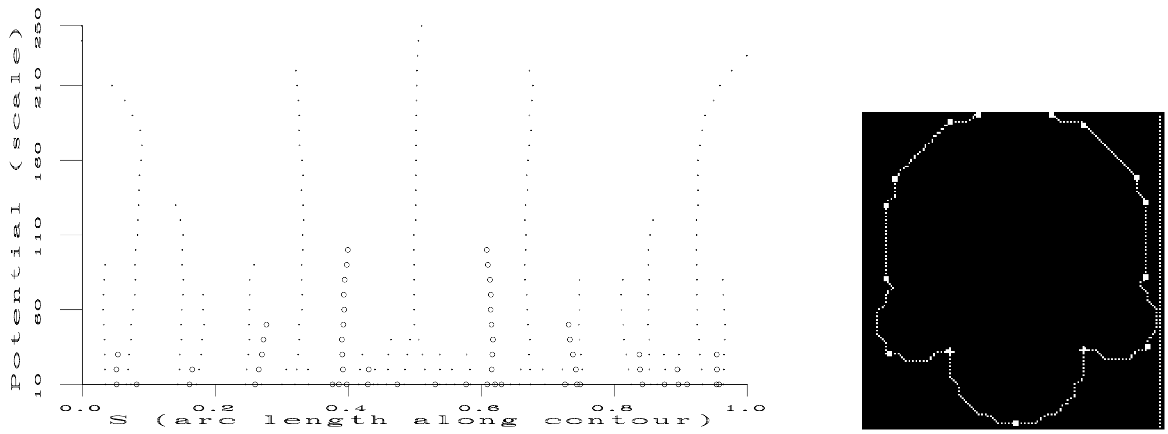

(a) (b)

Figure 21: Comparison with related work. A digital object consisting of a large semi-circle and 3 small semi-circles digitized from [25]. (a) the scale-space corner map of the object. (b) Corners detected are marked and superimposed on the object's boundary. The figure shows 13 convex corners and 2 concave corners are detected. Results compare favorably with results given in [21](Figure 22in [21]).

distribution. The interior Dirichlet boundary problem of the Poisson equation is then solved inside of the object giving rise to a potential distribution or surface of the object. Field extrema are then detected along equipotential contours resulting in a scale-space corner representation where the potential is the scale dimension. Correspondence between corners along equipotential contours are made starting at a given potential leading to the initial corner positions. Finally, the object's boundary is shot at from the initial corners' positions to locate the final corner locations.

Experiments have been conducted to show the effectiveness of the EFT-based approach. First, the EFT-based approach was applied to simple geometric shapes in the testing procedure to see the impact of quantization noise, corner angle, and corner orientation on the performance of the proposed corner detector. The detector has been shown to be quite robust and reliable. Then, the impact of boundary noise has been investigated systematically to show the accuracy of the proposed corner detector. The multiscale capability of the approach has been illustrated in an experiment where corners are detected at different levels of details. Finally, experiments have also been conducted to compare the proposed EFT-based corner detection approach with another recently proposed approach. All the experimental results are very encouraging.

The proposed approach has been shown to possess a number of desirable feature that can naturally solve many problems that are encountered in existing corner detection approaches. The EFT-based approach is parameter-free, robust, noise insensitive, accurate, and it possesses a multiscale capability. Moreover, since the proposed corner detection approach is developed based on a well-established theory, the EFT, the performance of the proposed approach under varying conditions can be predicted and justified even before experiments are conducted.

Our research work using the EFT framework for solving computer vision problems inspires further research using the same approach in addressing other vision problems. Many directions of research based on the EFT can be done. For example, the EFT has already been used successfully in solving the skeletonization problem [2]. The potential distribution or surface in its own constitutes a useful representation of objects at various levels of details similar to the multiscale curvature-based shape representation approach [17], [18]. In the proposed approach, scale is naturally defined by the potential distribution. In fact, the equipotential contours generated from the potential surface can be viewed as fingerprints of the object [19] for robust representation and recognition, the application of which is an interesting research topic.

One problem found with the EFT-based approach is that the potential distribution can have more than one peak for objects with narrow or *bottleneck* features. This means that more than one equipotential contour can be built for a certain potential value, and hence, will affect the results. The problem is not inherent to the EFT but iss a result of spatial quantization due to the presence of the bottlenecks. A possible solution to this problem is to use the multigrid approach [28] to refine the potential distribution in regions near the bottlenecks, the development of which is beyond the scope of this paper.

A natural extension to the EFT-based approach is to use it in representing three-dimensional objects because the Poisson equation is general and is not restricted to two dimensions. The potential surface becomes the *potential volume* and the equipotential contours are replaced by the equipotential surfaces. Also, the electrostatic field extrema would correspond to curvature extrema, and hence, three-dimensional edges and three-dimensional corners can be detected using the same methodology described in this paper.

Another extension to the approach is to extend it to solve the *dynamic scene analysis* problem. In this case, the more general *wave equation* can be used instead of the Poisson equation to model and accommodate for the time variation of the potential distribution.

The most critical step in the proposed approach in terms of the running time performance is the generation of the potential distribution. Non-iterative direct analytical methods for solving the Poisson equation [25] deserve further investigation.

The experience in this work suggests that interesting features exhibited by the EFT-based approach of corner detection and skeletonization promote the investigation of more physics-motivated models in solving computer vision problems. Finally, it is believed that borrowing simple ideas from other disciplines, such as physics, will definitely enrich research in the computer vision community.

References

[1] G. H. Abdel-Hamid and Y.-H. Yang, Electrostatic field-based detection of corners of planar curves, in *Proceedings of the 1993 Canadian Conference on Electrical and Computer Engineering*, Vancouver, Canada, Sept. 1993, pp. 767-770.

[2] G. H. Abdel-Hamid and Y.-H. Yang, Multiresolution skeletonization: an electrostatic field-based approach, *Proceedings of The IEEE International Conference on Image Processing (ICIP'94)*, Austin, Texas, USA, Nov. 13-16, 1994.

[3] H. Asada and M. Brady, The curvature primal sketch, *IEEE Trans. Patt. Anal. Machine Intell.*, vol. 8, no. 1, pp. 2-14, 1986.

[4] F. Attneave, Some informational aspects of visual perception, *Psychol. Rev.*, vol. 61, no. 3, pp. 183-193, 1954.

[5] K. J. Binns and P. J. Lawrenson, *Analysis and Computation of Electric and Magnetic Field Problems*, Pergamon Press, New York, 1963.

[6] G. Chen and Y. -H. Yang, Edge detection by regularized cubic B-spline fitting, Res. Rep. 91-8, University of Saskatchewan, Dept. of Comp. Sc. , Saskatoon, Saskatchewan, Canada, Aug. 1991, to appear in *IEEE Trans. Systems, Man, and Cybernet.*

[7] L. Drechler and H. Nagel, Volumetric model and 3-d trajectory of a moving car derived from monocular tv-frame sequence of a street scene, in *Proceedings IJCAI*, pp. 692-697, 1981.

[8] J. Q. Fang and T. S. Huang, A corner finding algorithm for image analysis and registration, *Proceedings AAAI Conf.*, pp. 46-49, 1982.

[9] H. Freeman and L. S. Davis, A corner-finding algorithm for chain-coded curves, *IEEE Trans. Comput.*, vol. 26, pp. 297-303, 1977.

[10] A. J. Baden Fuller, *Engineering Field Theory*, Pergamon Press, Oxford, 1973.

[11] M. A. Gennert, Detecting half-edges and vertices in images, in *Proceedings of IEEE Computer Society Conference on Computer Vision and Pattern Recognition*, pp. 552-557, 1986.

[12] L. Kitchen and A. Rosenfeld, Edge evaluation using local edge coherence, *IEEE Trans. Systems, Man, and Cybernet.*, vol. 11, No. 9, pp. 597-605, 1981.

[13] L. Kitchen and A. Rosenfeld, Gray level corner detection, *Pattern Recognition Lett.*, vol. 1, pp. 95-102, 1982.

[14] A. R. Mitchell and D. F. Griffiths, *The Finite Difference Method in Partial Differential Equations*, John Wiley, 1980.

[15] R. Mittra and S. W. Lee, *Analytical Techniques in The Theory of Guided Waves*, McMillan, New York, pp. 4-11, 1971.

[16] R. Mehrotra and S. Nichani, Corner detection, *Pattern Recognition*, vol. 23, no. 11, pp. 1223-1233, 1990.

[17] F. Mokhtarian and A. K. Mackworth, Scale-based description and recognition of planar curves and two-dimensional shapes, *IEEE Trans. Patt. Anal. Machine Intell.*, vol. 8, no. 1, pp. 34-43, 1986.

[18] F. Mokhtarian and A. K. Mackworth, A theory of multiscale curvature-based shape representation for planar curves, *IEEE Trans. Patt. Anal. Machine Intell.*, vol. 14, no. 8, pp. 789-805, 1992.

[19] M. A. Piech, Comment on fingerprints of two-dimensional edge models, *Comput. Vision, Graphics, and Image Process.*, vol. 42, pp. 381-386, 1988.

[20] K. Rangarajan, M. Shah, and D. V. Brackle, Optimal edge detector, *Comput. Vision, Graphics, and Image Process.*, vol. 48, pp. 230-245, 1989.

[21] A. Rattarangsi and R. T. Chin, Scale-based detection of corners of planar curves, *IEEE Trans. Patt. Anal. Machine Intell.*, vol. 14, no. 4, pp. 430-449, 1992.

[22] A. Rosenfeld and E. Johnson, Angle detection on digital curves, *IEEE Trans. Comput.*, vol. 22, pp. 875-878, 1973.

[23] A. Rosenfeld and J. S. Weazka, An improved method of angle detection on digital curves, *IEEE Trans. Comput.*, vol. 24, pp. 940-941, 1975.

[24] P. V. Sankar and C. V. Sharma, A parallel procedure for the detection of dominant points on a digital curves, *Comput. Vision, Graphics, and Image Process.*, vol. 7, pp. 403-412, 1978.

[25] T. Simchony, R. Chellappa, and M. Shao, Direct analytical methods for solving Poisson equations in computer vision problems, *IEEE Trans. Patt. Anal. Machine Intell.*, vol. 12, no. 5, pp. 435-446, 1990.

[26] I. N. Sneddon, *Elements of Partial Differential Equations*, McGraw-Hill, New York, 1957.

[27] C. Teh and R. T. Chin, On the detection of dominant points on digital curves, *IEEE Trans. Patt. Anal. Machine Intell.*, vol. 11, no. 8, pp. 859-872, 1989.

[28] D. Terzopoulos, Image analysis using multigrid relaxation methods, *IEEE Trans. Patt. Anal. Machine Intell.*, vol. 8, pp. 129-139, 1986.

[29] R. P. Winch, *Electricity and Magnetism*, Prentice-Hall, Englewood Cliffs, New Jersey, pp. 331-333, 1959.

[30] O. A. Zuniga and R. Haralick, Corner detection using the facet model, in *IEEE Proceedings CVPR*, pp. 30-37, 1983.